Lunar surface charging during solar energetic particle events: Measurement and prediction

J. S. Halekas,[1] G. T. Delory,[1] R. P. Lin,[1,2] T. J. Stubbs,[3,4] and W. M. Farrell[4]

Received 29 January 2009; revised 31 March 2009; accepted 9 April 2009; published 28 May 2009.

[1] We analyzed lunar surface charging during solar energetic particle (SEP) events, utilizing Lunar Prospector measurements of surface potentials and electron fluxes, and upstream energetic particle data. Outside of the magnetosphere, we find a nearly one-to-one correspondence between extreme negative lunar surface charging and large solar proton events. Using new techniques to correct for spacecraft potential, we present the first quantitative measurements of lunar charging during SEP events, during which we find that the nightside surface reaches potentials of up to −4.5 kV, with negative potentials of a kilovolt or larger often observed. These potentials are far higher than typical nightside potentials of a few hundred volts negative and may increase the risk of electrostatic discharge and/or dust effects, introducing an additional hazard to the already dangerous radiation environment. For eight of eleven event periods, surface potentials correlate with electron temperature and with the ratio of energetic electron flux to both energetic proton flux and total electron flux. For these eight events, charging models taking into account both thermal/suprathermal and energetic particle fluxes, as well as secondary emission, can successfully predict surface potentials. However, during the other three events, surface potentials do not correlate with the same measurable quantities, and charging models cannot reproduce measured potentials. In order to develop reliable and accurate models for lunar surface charging during SEP events, we will need better measurements of ion and energetic particle behavior in the lunar environment, secondary electron emission from lunar materials, and lunar surface potentials.

Citation: Halekas, J. S., G. T. Delory, R. P. Lin, T. J. Stubbs, and W. M. Farrell (2009), Lunar surface charging during solar energetic particle events: Measurement and prediction, *J. Geophys. Res.*, *114*, A05110, doi:10.1029/2009JA014113.

1. Introduction

1.1. Lunar Surface Charging

[2] The Moon has a tenuous exosphere and only weak and localized crustal magnetic fields, leaving most of its surface exposed to solar ultraviolet (UV) and X rays as well as solar and magnetospheric plasma and energetic particles, all of which affect lunar surface charging. Electron and ion impacts contribute negative and positive charging currents to the surface respectively, and can each also produce an escaping flux of secondary electrons (a positive charging current). Photon impacts generate an escaping flux of photoelectrons, also a positive charging current. Each of these charging currents depends on the electrostatic potential of the surface with respect to the surrounding plasma. The Moon, like any body in space, charges to an equilibrium potential such that the charging currents to its surface balance. Given the low lunar surface conductivity [*Schwerer et al.*, 1974], especially on the night side [*Alvarez*, 1977], each portion of the lunar surface should charge independently, and charging currents need only balance locally. Meanwhile, lunar surface charge densities and charging currents are such that the surface should respond rapidly ($\ll$1 s) to changes in solar illumination or plasma properties, quickly reaching an equilibrium potential.

[3] During its orbit around the Earth, the Moon is exposed to highly variable charging currents. The terrestrial magnetosphere contains very rarefied plasma in the tail lobes, with denser and more energetic plasma in the plasma sheet and magnetosheath regions. The solar wind consists of relatively cool streaming plasma, while the lunar wake (which forms downstream of the Moon in the solar wind) contains more energetic and much more rarefied plasma. During solar energetic particle (SEP) events, meanwhile, high fluxes of very energetic particles can impact the Moon. In addition, solar illumination, and therefore photoelectron current from the surface, depends on solar zenith angle (SZA) on the dayside. Commensurate with this variability in charging currents, lunar surface potentials can vary over orders of magnitude.

[4] On the sunlit hemisphere of the Moon, photoelectron currents usually dominate, and the surface charges to a small positive potential. On the night side, currents from

[1]Space Sciences Laboratory, University of California, Berkeley, California, USA.
[2]Physics Department, University of California, Berkeley, California, USA.
[3]Goddard Earth Sciences and Technology Center, University of Maryland, Baltimore, Maryland, USA.
[4]Solar System Exploration Division, NASA Goddard Spaceflight Center, Greenbelt, Maryland, USA.

Copyright 2009 by the American Geophysical Union.
0148-0227/09/2009JA014113

plasma electrons tend to dominate, and the surface charges to a negative potential. However, secondary electron emission can complicate matters by providing an additional positive current source, and given large enough secondary emission the nightside surface could even charge positive. LP measurements of secondary electron emission from lunar regolith [*Halekas et al.*, 2009], however, suggest that the nightside surface should usually remain negative. Simple charging theory predicts an equilibrium positive potential in sunlight on the order of a few times the photoelectron temperature and an equilibrium negative potential in shadow on the order of a few times the electron temperature (which can vary over orders of magnitude) [*Whipple*, 1981; *Stubbs et al.*, 2007b; *Manka*, 1973]. Apollo era and Lunar Prospector (LP) observations generally confirm these expectations [*Halekas et al.*, 2008]. In particular, LP observes the largest negative lunar surface potentials during plasma sheet crossings and SEP events, when the Moon is exposed to energetic ("high temperature") plasma.

1.2. Lunar Prospector Observations

[5] Previous studies [*Halekas et al.*, 2002, 2003, 2005a, 2007, 2008] have used Lunar Prospector Electron Reflectometer (LP ER) data to explore the charging of the lunar surface in various environments, by utilizing the electrons measured at spacecraft altitude as a remote probe of the lunar surface potential. Negative charging of the lunar surface affects electron distributions measured at spacecraft altitude in two ways. First, radial electric fields force energy-dependent electron reflection. For adiabatic reflection due only to magnetic fields, the fraction of the incident electron flux reflected before reaching the surface does not depend on energy. However, LP observations instead show energy-dependent reflection, indicating the presence of a potential drop between the spacecraft and the surface [*Halekas et al.*, 2002]. In addition, LP often observes beams of electrons traveling upward along magnetic field lines from the surface. These represent low-energy secondary electrons emitted from the surface and accelerated upward to the spacecraft by negative radial electric fields near the surface [*Halekas et al.*, 2002]. One can use either of these features of the electron distribution to remotely sense negative lunar surface potentials.

1.3. Spacecraft Charging

[6] In order to utilize LP ER measurements (which determine the potential drop between the spacecraft and the surface) to infer the lunar surface potential, one must first understand the charging of the spacecraft itself. The methods previously used to determine the LP spacecraft potential in both sunlight and shadow by *Halekas et al.* [2008] relied purely on LP electron measurements. In sunlight, when the spacecraft charges positive, one can use the break in the measured electron spectrum between spacecraft photoelectrons and plasma electrons to determine the spacecraft potential. For negative spacecraft charging in shadow, on the other hand, one cannot rely on photoelectrons or any other secondary population to determine the spacecraft potential. Instead, *Halekas et al.* [2008] developed a spacecraft charging model by fitting the electron distribution measured by LP to a kappa function, assuming equal ion and electron densities and temperatures, assuming a secondary electron emission yield function, and then parameterizing the spacecraft potential by the electron temperature and the kappa index of the electron kappa distribution. The authors then calibrated the charging model and determined the spacecraft secondary yield function by comparing electron distributions in quiet regions and requiring continuity across the light/shadow boundary. *Halekas et al.* [2008] utilized this method to determine that the LP spacecraft, assuming a Sternglass secondary electron yield function $\delta(E) = 7.4\delta_m E/E_m \bullet \exp(-2\sqrt{E/E_m})$ [*Sternglass*, 1954], has a maximum secondary yield of $\delta_m = 1.5$ at a primary electron energy $E_m = 500$ eV.

[7] The most recent analysis of LP ER data, which for the first time utilized this spacecraft charging model to correct for spacecraft potential, and also self-consistently utilized the entire electron distribution to determine lunar surface potentials, found typical nightside lunar surface potentials of a few hundred volts negative or smaller in the terrestrial magnetotail lobes and in the lunar wake [*Halekas et al.*, 2008]. However, during plasma sheet crossings and SEP events, LP has observed much larger negative surface potentials.

1.4. Extremes in Lunar Surface Charging

[8] In the plasma sheet, on the night side and occasionally even on the dayside, lunar surface potentials can reach $\sim -1-2$ kV [*Halekas et al.*, 2005a, 2008]. Meanwhile, during SEP events, LP has observed nightside lunar surface potentials as large as ~ -4.5 kV [*Halekas et al.*, 2007, 2008]. However, to date, no one has corrected LP surface potential measurements during SEP events for the effects of spacecraft charging. Previous methods of determining and correcting for the effects of the LP spacecraft potential relied only on LP ER measurements of the electron distribution [*Halekas et al.*, 2008]. During time periods with large fluxes of energetic particles (such as SEP events), we cannot use these previously developed methods, because energetic particles can also contribute significantly to the spacecraft current balance. Therefore previous measurements of lunar surface potentials during SEP events have an unknown offset due to spacecraft charging.

[9] Quantitative measurements of surface charging during SEP events may prove important, because kilovolt-scale surface potentials could have potentially significant consequences for robotic and/or human lunar surface exploration. Spacecraft charging and electrostatic discharge historically constitute the leading causes of spacecraft failures in orbit [*Bedingfield et al.*, 1996; *Koons et al.*, 2000; *Leach*, 1995], and could also impact operations on the lunar surface. Charging during SEP events could prove even more hazardous because of the combination of enhanced charging and radiation. SEP events can produce large amounts of radiation, with up to half of all energetic particles that strike the Moon during a solar cycle arriving during a few large events [*Adams and Shapiro*, 1985]. Meanwhile, the same charging processes that affect the surface also influence individual dust grains. If surface electric fields can overcome surface cohesive forces, they could lift charged dust grains form the surface and transport them vertically and/or laterally [*Stubbs et al.*, 2006, 2007c]. We cannot easily predict the extent of hazards to exploration from charged dust, but significant hazards could result from dust [*Stubbs*

et al., 2007a]. All of these considerations provide us with ample reason to investigate lunar charging during SEP events.

[10] In this study, we first develop new techniques to determine the spacecraft potential during SEP events, utilizing upstream measurements of energetic electron and ion fluxes in addition to LP electron measurements. These techniques allow more accurate measurements of lunar surface charging during SEP events. We then use these new corrected results to investigate the charging of the lunar surface during SEP events, as observed in 1998 by LP, both qualitatively and quantitatively. We investigate correlations between observed surface potentials and all relevant measurable plasma parameters, in order to determine which factors control lunar surface charging during SEP events. Finally, we develop several surface charging models and compare them to our measurements, with the goal of working toward a predictive capability for lunar surface charging during SEP events.

2. Data Sources

[11] This study utilizes measurements made in 1998 by the Lunar Prospector Electron Reflectometer (LP ER) to determine lunar electrostatic potentials and measure the electron spectrum around the Moon. The ER was a top-hat electrostatic analyzer capable of measuring full three-dimensional electron distribution functions from a few eV to 20 keV. During the time period considered in this study, the analyzer energy sweep covered electron energies of 38 eV to 17 keV (center energies for each energy bin). The analyzer had an intrinsic energy resolution of $\Delta E/E = \sim 0.25$, but the onboard processor summed adjacent energy bins together, resulting in an effective $\Delta E/E = \sim 0.5$. LP had a rapidly precessing polar orbit ($\sim$2 hr period), allowing full coverage of the lunar surface twice a month. LP orbited at $\sim$100 km altitude for the entire time period considered in this study. In its orbit around the Earth, the Moon spends $\sim$75% of the time in the solar wind, and the rest in the terrestrial magnetosheath and geomagnetic tail (including tail lobes and plasma sheet). We only consider solar wind time periods in this paper (during which the LP spacecraft orbits through the solar wind and lunar wake).

[12] We also utilize upstream data from Wind, ACE, and SOHO to determine energetic particle fluxes. For these measurements, we rely on key parameter data from the SOHO COSTEP (500 keV to 7.4 MeV electrons, 540 keV to 47 MeV protons), Wind EPACT (19–72 MeV protons), ACE EPAM (38–315 keV electrons, 47 keV to 4.75 MeV protons), and ACE SIS (>10 MeV protons) experiments [*Muller-Mellin et al.*, 1995; *von Rosenvinge et al.*, 1995; *Gold et al.*, 1998; *Stone et al.*, 1998].

3. Determining the Spacecraft Potential during SEP Events

[13] To accurately determine the magnitude of the lunar surface potential during SEP events, we mainly need to understand the negative spacecraft potentials achieved in shadow, which can greatly exceed any positive spacecraft potentials achieved in sunlight. Unfortunately, the techniques previously used to determine negative spacecraft potentials [*Halekas et al.*, 2008] relied on the electron and ion distributions each having a simple one-component form. During SEP events, both ion and electron distributions can have multiple components, and LP electron measurements cannot completely characterize the electron distribution. Instead, we must also consider both energetic ion and electron measurements. To accomplish this, we utilize upstream measurements from Wind, ACE, and SOHO, and assume that the same energetic particle fluxes impact the lunar environment. One expects the presence of the solid lunar obstacle to reduce the energetic particle flux at some locations around the Moon. However, LP electron data show only a small reduction in electron flux in the lunar wake even at a comparatively low energy of 17 keV, so we expect that fluxes of more energetic particles around the Moon should not differ greatly from upstream values. The gyroradii of these particles are large and their velocities large, and they should generally penetrate efficiently into the wake region. For very small-scale structures in the solar wind and/or very anisotropic particle fluxes, this expectation may not hold true, but for most times it should prove adequate.

[14] To determine negative spacecraft potentials during SEP events, we first characterize the low-energy portion of the electron distribution, and use the electron parameters thus determined as inputs to approximate the expected thermal proton flux. We begin by fitting the low-energy (below 2 keV) portion of the thermal/suprathermal electron distribution measured by the LP ER to a kappa function with the form

$$f_E(v) = \frac{\Gamma(\kappa+1)}{(\pi\kappa)^{3/2}\Gamma(\kappa-1/2)}\frac{n_{FIT}}{\Theta^3}\left[1+v^2/\left(\kappa\Theta^2\right)\right]^{-\kappa-1}, \qquad (1)$$

with kappa index κ, electron density n_{FIT}, and electron temperature at the spacecraft (inside the sheath) equal to $T_{\mathrm{FIT}} = \kappa/(\kappa - 3/2) \bullet \mathrm{m}\Theta^2/(2k)$ (with m the electron mass and Θ the thermal velocity). To determine the corresponding electron density and temperature outside of the sheath in the surrounding plasma, we shift the distribution of equation (1) by the (unknown) spacecraft potential. Given a kappa function distribution, we can solve to find the ambient plasma density and temperature $n_{\mathrm{E}} = n_{\mathrm{FIT}}\,[1 + \frac{eU_{LP}}{kT_{FIT}(\kappa-3/2)}]^{1/2-\kappa}$ and $kT_E = kT_{\mathrm{FIT}} + eU_{LP}/(\kappa - 3/2)$, with $\mathrm{U_{LP}}$ the unknown spacecraft potential (E = electrons, I = protons). Using these parameters, we can then calculate the expected ambient thermal proton spectrum, assuming a Maxwellian distribution

$$f_I(v) = n_I \bullet (m/(2\pi kT_I))^{3/2}\exp\left[-mv^2/(2kT_I)\right], \qquad (2)$$

with proton density and temperature equal to electron density and temperature ($\mathrm{n_I} = n_{\mathrm{E}}$, $\mathrm{T_I} = T_{\mathrm{E}}$). Quasineutrality is always a good approximation in space plasma physics; however the assumption of equal temperatures may not always hold. Luckily, the spacecraft potential, which depends mainly on the balance between primary and secondary electrons in the wake, does not depend strongly on the proton temperature. We found that changing the proton temperature by a factor of ten only changed the predicted spacecraft potential by an average of $\sim$30% or less in most cases. In the lunar wake, thermal proton distributions may prove considerably more

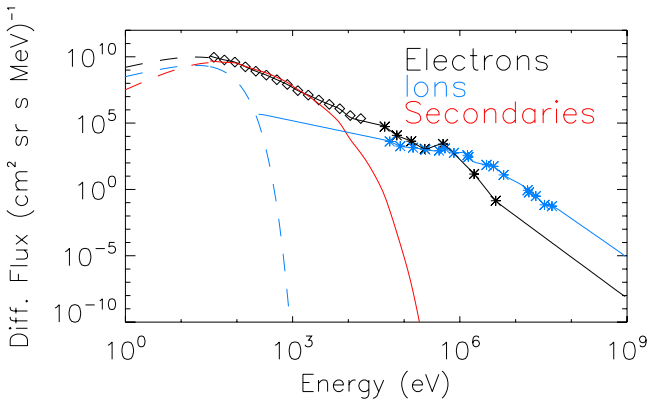

Figure 1. Electron and proton spectra measured by LP and upstream monitors at 1998/05/06/20:57 (during Event 5), along with extrapolations and modeled secondary electron spectrum. Black diamonds show LP electron data; black asterisks, upstream electron data; and blue asterisks, upstream proton data. Black line shows electron spectrum, including power law extrapolation at high energies (solid), and extrapolation from kappa function fit at low energies (dashed). Dashed blue line shows assumed low-energy Maxwellian distribution for thermal protons. Solid blue line shows proton spectrum, including power law extrapolations at low and high energies. Red line shows modeled secondary electron flux. Fit to electron distribution gives $\kappa = 2.24$, $n_{FIT} = 0.03$ cm^{-3}, $T_{FIT} = 54.6$ eV. For a spacecraft potential of -27 V, these values imply $n_E = 0.21$, $T_E = 18.1$. These values of density, temperature, and spacecraft potential imply a thermal proton directional number flux at the spacecraft of 8.8×10^5 cm^{-2} s^{-1}, which together with the non-thermal proton flux of 4.6×10^3 cm^{-2} s^{-1} and the secondary electron flux of 2.6×10^6 cm^{-2} s^{-1}, roughly balance the total electron flux of 3.4×10^6 cm^{-2} s^{-1}.

complicated than the simple distribution of equation (2) considered here; however, absent direct measurements, we adopt the simplest possible model in this study.

[15] We calculate the thermal proton directional number flux to the charged spacecraft (as a function of the unknown spacecraft potential) from the distribution of equation (2), using

$$J_I = n_I\sqrt{\frac{kT_I}{2\pi m_I}}\left[1-\frac{\mathrm{eU_{LP}}}{\mathrm{kT_I}}\right] \equiv n_E\sqrt{\frac{kT_E}{2\pi m_I}}\left[1-\frac{\mathrm{eU_{LP}}}{\mathrm{kT_E}}\right]. \quad (3)$$

equation (3) assumes thick-sheath charging, since we expect a Debye scale large in comparison to the spacecraft size ($\lambda_D \gg R_{LP}$). Therefore the negatively charged spacecraft attracts ions from the sheath region that would not otherwise have impacted the spacecraft. This accounts for the factor of (1-eU$_{LP}$/kT) compared to the directional flux from a Maxwellian distribution near an uncharged surface [*Horányi*, 1996; *Whipple*, 1981].

[16] Next, we construct the full electron spectrum at the spacecraft over the energy range from zero to 1 GeV, using LP and upstream measurements, and interpolating and extrapolating where necessary. We perform a basic background subtraction on the LP electron data in order to remove the background signal from all penetrating particles. We utilize a power law extrapolation at high energies, and use the kappa function fit determined above (converted from distribution function f(v) to differential number flux dJ(E)/dE) to extrapolate to energies below the LP energy sweep.

[17] Similarly, we construct the non-thermal proton spectrum at the spacecraft, using upstream measurements, and utilizing power law extrapolations up to 1 GeV and down to the region covered by the Maxwellian thermal proton distribution determined above.

[18] Finally, we calculate the secondary emission spectrum using the spacecraft secondary yield function determined by *Halekas et al.* [2008] and described above, and numerically integrating this yield over the full electron spectrum determined above in order to determine the secondary electron spectrum from the spacecraft.

[19] Figure 1 shows example electron, proton, and secondary electron spectra determined using these methods. From each of these spectra, we can calculate total directional number fluxes, integrating (assuming isotropic distributions) to find $J_{PRIMARY_I,E} = \pi\int\frac{dJ_{I,E}(E)}{dE}dE$ (E = electrons, I = protons) and $J_{SECONDARY} = \pi\int\frac{dJ_E(E)}{dE}\delta(E)dE$. Finally, we vary the assumed spacecraft potential and repeat the entire set of calculations described above for a wide range of assumed potentials to find the spacecraft potential U_{LP} at which the sum of the proton thermal and energetic directional fluxes (positive), secondary electron directional fluxes (positive), and primary electron directional fluxes (negative) balance. We determine the point of current balance by finding the minimum in the total flux divided by the primary electron flux, as shown in Figure 2.

[20] On the dayside, in sunlight, we take into account two extra currents, corresponding to the solar wind ion flow toward and the photoelectron flux from the sunlit side of the spacecraft. We assume a typical spacecraft photoelectron current of 50 μA/m^2, and a solar wind velocity of 400 km/s. In practice, the spacecraft almost always charges to small positive values in sunlight, for a wide range of these parameters.

[21] This new technique for determining negative spacecraft potentials during SEP events is much more general

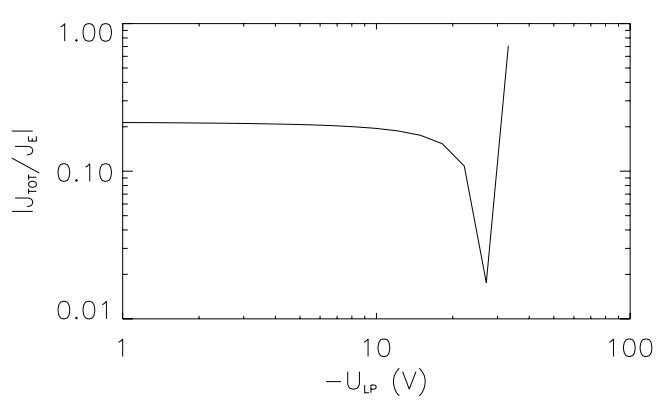

Figure 2. Magnitude of total flux to the spacecraft divided by electron flux to the spacecraft at 1998/05/06/20:57, as a function of assumed negative spacecraft potential, showing a minimum at ~-27 V spacecraft potential, with a FWHM of $\sim$5V, for an error of $\sim$2.5 V.

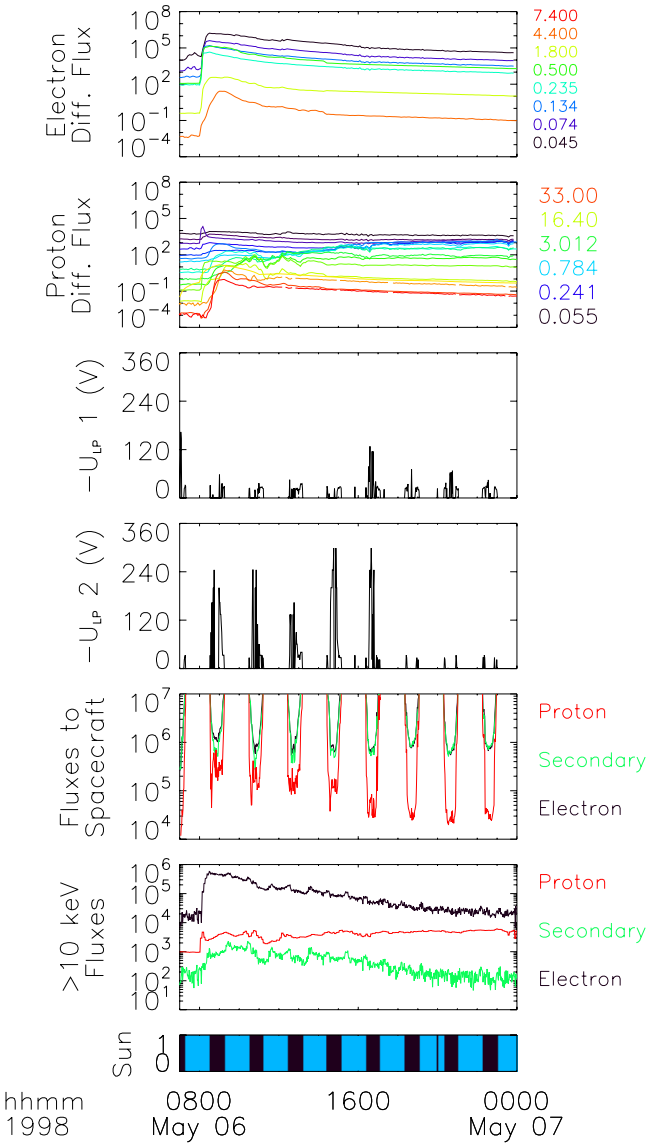

Figure 3. Upstream energetic electron and proton differential fluxes, magnitude of negative spacecraft potential calculated using two different techniques, and integrated total charged particle fluxes to/from the spacecraft, for a time period during Event 5. Total fluxes at the spacecraft (inside the sheath) shown for protons, electrons, and secondary electrons of all energies and of/produced by primary particle energies greater than 10 keV. The first technique (U_{LP} 1) utilizes only electron data from LP, while the second (U_{LP} 2) takes into account energetic particles. Particle energies displayed in MeV, differential fluxes in $(cm^2\ s\ sr\ MeV)^{-1}$, total fluxes in $cm^{-2}\ s^{-1}$. Bottom bar shows sun/shadow at LP (blue, sun; black, shadow).

than that of *Halekas et al.* [2008], since it takes into account the entire electron and proton distributions, including energetic particles, and allows us to more accurately treat negative spacecraft charging in the presence of multicomponent distributions. During quiet times, the new technique agrees closely with previously utilized methods; however, during SEP events, we now predict larger negative spacecraft potentials at some times, as shown in Figure 3. For this period, we clearly see the effect of the huge increase in energetic electron fluxes in the first half of the time range shown, which forces the spacecraft to charge more negatively in order to pull in more thermal protons from the sheath region to balance the currents to the spacecraft. Even for these large energetic electron fluxes, however, the balance between low-energy electrons and secondary electrons remains an important factor, as indicated by the fact that the spacecraft potential does not decrease monotonically with the energetic electron fluxes. For this event, energetic proton fluxes do not contribute substantially to the charging balance; however, at some times, energetic protons also play an important role in spacecraft charging. The period shown in Figure 3 represents an extreme case; only for a few events with very large increases in energetic electron fluxes does the spacecraft potential reach negative values as large as these.

4. Measuring the Lunar Surface Potential During SEP Events

[22] Previous LP measurements of lunar surface charging have utilized both energy-dependent electron reflection and secondary electrons accelerated from the surface to remotely sense the magnitude of negative surface potentials. For this work, to ensure good coverage during SEP events, even in the presence of sometimes substantial penetrating particle background, we have followed the methodology of *Halekas et al.* [2007] and used measurements of accelerated beams of secondary electrons to remotely sense the surface potential. We utilize the same automated software developed in that study to find upward traveling beams, and manually check each beam thus identified to ensure data quality. The energy of the secondary electron beam provides a measure of the potential drop $\Delta U = U_M - U_{LP}$ between the spacecraft and the surface (with a resolution equivalent to the LP ER instrumental energy resolution of ~50%). By adding the spacecraft potential U_{LP}, as determined in the previous section, we therefore obtain a measurement of the lunar surface potential U_M.

[23] In practice, the correction for spacecraft potential usually proves relatively small, with the lunar surface reaching much larger potentials than the spacecraft. This disparity in charging behavior likely arises both from the different material properties and from the different scale sizes of the spacecraft and Moon as compared to the Debye scale. The spacecraft apparently has a greater secondary electron yield than lunar regolith materials, thereby reducing the magnitude of negative surface potentials. The spacecraft also has a thick sheath compared to its scale size, and therefore attracts additional ions to its negatively charged surface, moderating the magnitude of negative spacecraft potentials. On the other hand, the Moon has a very thin sheath compared to its scale size, limiting the ion current to the negatively charged surface, and allowing its surface to reach much larger negative potentials.

5. Systematics of Lunar Surface Charging During SEP Events

[24] We use the techniques described above to characterize all periods during which LP observed negative lunar

Table 1. Event List for 1998

Event No.	Time Period Considered	NOAA Solar Proton Event[a]	GEO SPE Start Time	GEO SPE Peak Time	GEO/L1 Peak Proton Flux (>10 MeV)[b]	L1 Peak Proton Diff. Flux (1.91–4.75)[c]	L1 Peak Electron Differential Flux (0.175–0.315)[c]	Peak Lunar Surface Potential (V)	GSE Angle of Moon
1	04/20/00:00–04/23/00:00	20 April	14:00	04/21/12:05	1700/1600	3e2	1e5	−1400	272–311
2	04/30/00:00–05/01/21:00					1e2	7e2	−500	48–71
3	05/01/21:00–05/04/00:00	2 May	14:20	05/02/16:50	150/120	1e2	1e4	−1500	71–97
4	05/04/00:00–05/06/00:00					7e2	1e3	−800	97–119
5	05/06/00:00–05/08/00:00	6 May	08:45	05/06/09:45	210/400	2e2	5e4	−4500	119–140
6	08/24/00:00–08/28/00:00	24 August	23:55	08/26/10:55	670/NA	5e3	5e4	−1900	22–66
7	09/24/00:00–09/26/00:00	25 September	00:10	09/25/01:30	44/23	3e3	9e2	−500	36–58
8	09/26/00:00–09/28/00:00					20	4e3	−1200	58–80
9	09/28/00:00–09/30/12:00					10	1e3	−1900	80–109
10	09/30/12/00–10/03/00:00	30 September	15:20	10/01/00:25	1200/720	8e2	2e4	−2000	109–141
N/A	N/A	8 November	02:45	11/08/03:00	11/7	3e2	3e2	N/A	234
11	11/13/00:00–11/16/00:00	14 November	08:10	11/14/12:40	310/190	70	2e4	−1300	293–325

[a]From NOAA list of solar particle events that affected the terrestrial environment in 1998 http://www.swpc.noaa.gov/ftpdir/indices/SPE.txt.
[b]Peak total proton flux above 10 MeV in $(cm^2\ s\ sr)^{-1}$ measured by GOES at geosynchronous (GEO) and by ACE SIS at L1.
[c]Peak differential proton and electron fluxes in $(cm^2\ s\ sr\ MeV)^{-1}$ at selected energies measured at L1 by ACE EPAM.

surface potentials larger than 500 volts in the solar wind, outside of the terrestrial magnetosphere. We separate these charging events into five time periods in April, May, August, September/October, and November 1998 (separated by thick black lines in Table 1), and further sub-divide some of these time periods to arrive at a final list of 11 event periods for further study, as shown in Table 1 and displayed in Figures 4 and 5. These extreme charging time periods correlate very well with periods when other spacecraft observe large energetic proton fluxes in the upstream solar wind and at geosynchronous altitude, as shown in Table 1. Indeed, we find a nearly one-to-one correlation between extreme charging events observed by LP and a NOAA list of solar proton events that affected the Earth's space environment in 1998 (this list also corresponds to the periods with the highest energetic proton fluxes upstream, outside of the magnetosphere, likely more relevant to the charging environment for the Moon in the solar wind). Only the 8 November solar proton event (the smallest on the NOAA list, also shown in Table 1 for completeness) does not correspond to an extreme surface charging event. During the 8 November event, as suggested by the GSE angle of the Moon and also by more careful examination of the magnetic field during this time period, the Moon may lie at the edge of the terrestrial magnetosheath, complicating the charging current balance picture. Alternatively, this event may simply have proven too small to significantly affect the lunar charging during this time period. In any case, all other large solar proton events observed near the Earth in 1998 correlate directly with periods of enhanced lunar charging observed by LP, as shown in Table 1.

[25] These large solar proton events, which appear to directly control lunar surface charging, are very diverse in nature. According to the NOAA list referenced in Table 1, and *Kahler* [2005], only the April and May events can be clearly associated with large CMEs. However, upstream monitors do observe forward interplanetary shocks associated with the April and May events, and also with the August, September/October, and November events [*Howard and Tappin*, 2005]. ACE also observed fast ejecta and shocks on 1 May, 3 May, 4 May, 24 September, and 8 November [*Burlaga et al.*, 2001].

[26] Some of the solar proton events considered here have been previously studied in great detail, with particular attention paid to the April and May events (Events 1–5, see Table 1 and Figure 4), the first large events and the first strongly geoeffective interval in solar cycle 23 [*Farrugia et al.*, 2002]. This time period has as many as three full halo CMEs and three partial CMEs [*Burlaga et al.*, 2001]. Wind and ACE observe three interplanetary shocks which also correspond to increases in low-energy electron flux observed by LP during Events 2 and 3, as well as several directional discontinuities, including one associated with another large increase in low-energy electron flux measured by LP at the beginning of Event 4 [*Farrugia et al.*, 2002]. A large magnetic cloud, trailed by a hot fast (~900 km/s) flow [*Farrugia et al.*, 2002] passes 1 AU during Event 3, and a large SEP event injects energetic particles into this structure [*Malandraki et al.*, 2002]. This event has exceptionally anisotropic proton fluxes, and it appears that the magnetic cloud structure provides a "highway" for energetic particles [*Torsti et al.*, 2004]. Finally, another SEP injection, with

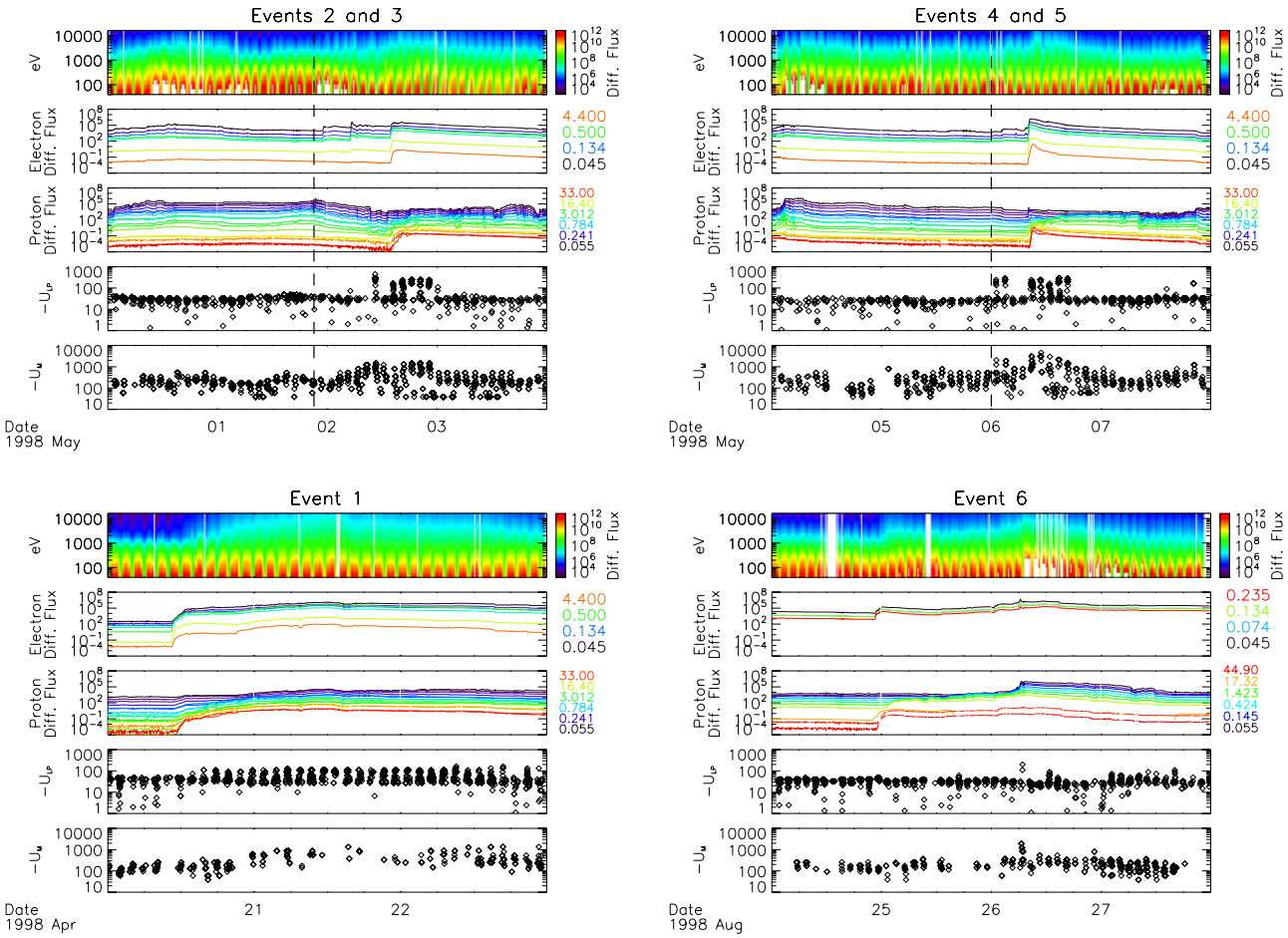

Figure 4. Particle differential fluxes and lunar potentials for Events 1–6. Images show LP electron data, upstream energetic electron and proton data, magnitude of negative spacecraft potential, and magnitude of negative lunar surface potential. LP electron energies displayed in eV, energetic particle energies in MeV, differential fluxes in $(\mathrm{cm}^2\ \mathrm{s\ sr\ MeV})^{-1}$. Line colors for energetic particle data vary from event to event.

characteristics of both impulsive and gradual events [*von Rosenvinge et al.*, 2000] occurs during Event 5. At the Moon, we observe kilovolt-scale surface potentials on the night side during both the gradual injection of SEPs in April (Event 1) and the two relatively more impulsive injections in May (Events 3 and 5). Events 2 and 4 also show some increases in energetic particle fluxes and surface potentials, but with lower levels of both, commensurate with the absence of a large SEP injection during these two time periods.

[27] The remaining events (Events 6–11, see Table 1 and Figures 4–5) have not received as much attention in previous studies, but include a number of interesting events, including several large SEP injections. In August (Event 6) we observe a brief spike in the surface potential associated with the energetic particles observed during the passage of a shock front, but not with the earlier SEPs. We observe very strong charging during one SEP injection (Event 10) in September/October, but more moderate charging during the other one (Event 7). We also observe rather large potentials associated with increased energetic electron fluxes (but with no corresponding increase in energetic proton fluxes) during Event 8 and 9 in September/October. Finally, in November (Event 11), we observe a brief charging enhancement associated with the initial SEP injection, but not during the following time period (during which energetic particle fluxes remained enhanced).

[28] Despite the clear correspondence between extreme lunar surface charging and large solar proton events demonstrated in Table 1 and Figures 4–5, we do not find an obvious correlation between the peak surface potential and the peak energetic electron or proton fluxes at any given energy, or with the position of the Moon with respect to the Earth. Peak electron differential fluxes and surface potentials do seem to correlate to some degree, as one might expect (since greater fluxes of energetic electrons should produce larger surface potentials), but this correlation does not hold for all events. For instance, during Events 8 and 9, electron fluxes remained relatively small compared to other SEP events, but the lunar surface still charged to large negative potentials. The ratio of electron to proton fluxes (large during these two event periods, during which we observed hardly any energetic protons) may prove as or more important. In order to determine which factors actually control lunar surface charging during these SEP events, we investigate in more detail in the following sections, by

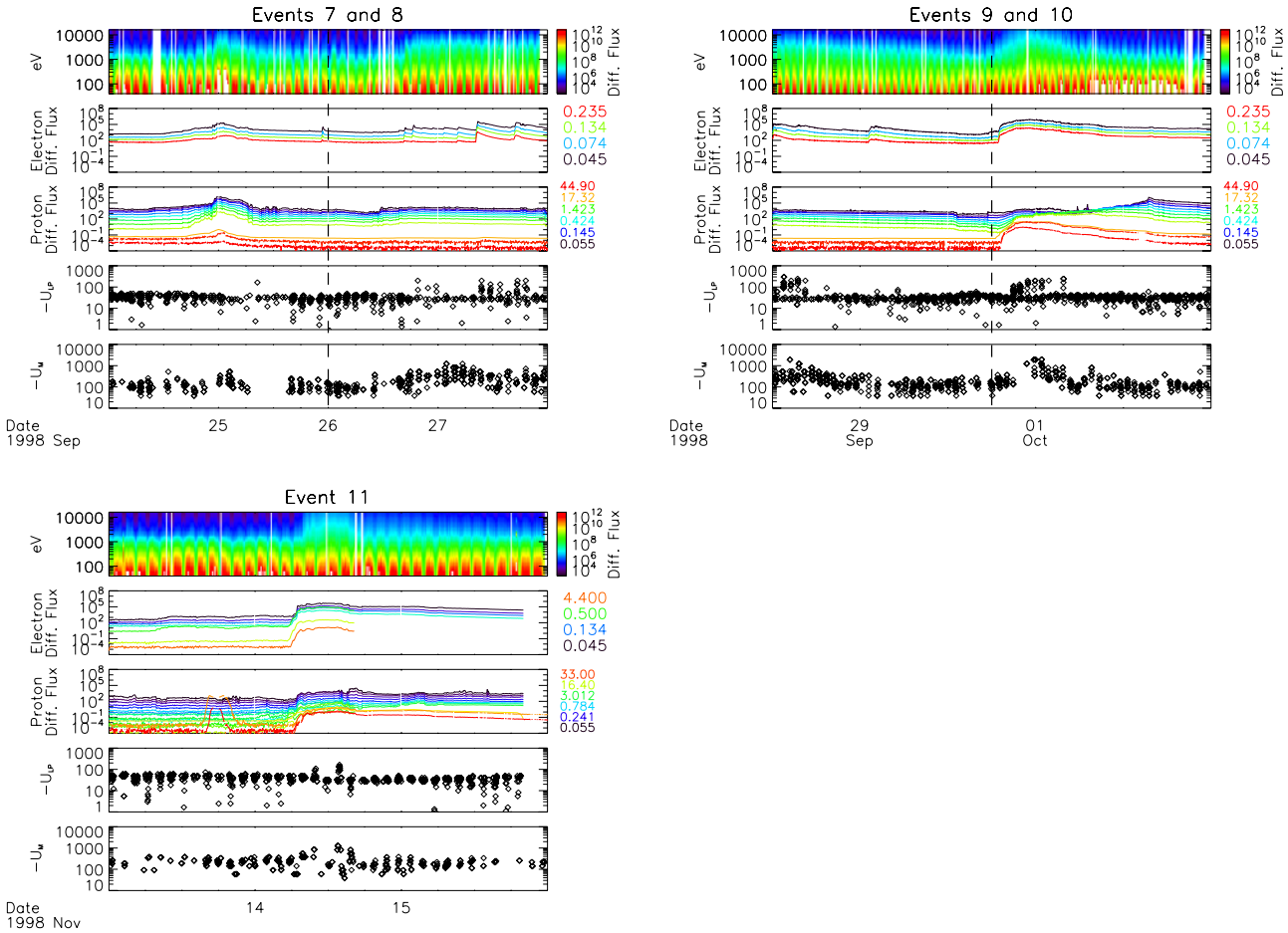

Figure 5. Particle fluxes and lunar potentials for Events 7–11. All images same as in Figure 4.

considering the relevant quantities observed throughout each event, rather than just the peak potentials and fluxes.

6. Correlating Surface Potentials With Relevant Measurable Quantities

[29] In order to work toward a predictive capability, we investigate correlations between the magnitude of measured lunar surface potentials and other measurable parameters, for each event period. We consider all major current sources except for secondary emission. Since we have no way of measuring or estimating the secondary emission current from the surface without prior knowledge of the lunar surface potential, we cannot investigate this parameter or use it for predictive purposes without employing more sophisticated modeling (as in the following section). We use essentially the same procedure developed in section 3 to construct input electron and proton spectra (corrected for spacecraft potential) covering all energies up to 1 GeV (as shown in Figure 1). We only consider nightside data in this portion of our investigation, and we only utilize the downward going portion of the electron distribution, since only this portion can affect the Moon.

[30] We utilize rank correlations rather than simple cross-correlations. To calculate the Spearman rank correlation, one orders all observations by magnitude and assigns them a rank corresponding to that order, then calculates a correlation between those rank numbers [*Press et al.*, 1992]. We found the rank correlation more useful for identifying causal relationships between quantities that vary over many orders of magnitude, especially with outliers present. We correlate the magnitude of the negative lunar surface potential with the density n_E, temperature T_E and kappa index κ_e of the thermal/suprathermal portion of the electron distribution, calculated from a kappa function fit to the downward going electron spectrum below 2 keV. We also correlate with total electron flux J_e, total proton flux J_i, electron flux above 10 keV J_{e_hi}, proton flux above 10 keV J_{i_hi}, and selected ratios of these fluxes. We calculate all of these parameters at LP spacecraft altitude, corrected for spacecraft potential where necessary in order to determine the values appropriate for the ambient plasma. Where appropriate, we also calculate the corresponding parameters at the lunar surface by shifting the electron spectrum by the surface potential and recalculating the relevant quantities. The proton current to the lunar surface stays constant, since given the Moon's large size compared to the Debye scale (which ensures the validity of a thin-sheath approximation) proton fluxes will remain constant between the spacecraft and the negatively charged surface; the energy of protons reaching the surface will increase, but their density will decrease correspondingly, resulting in flux conservation. We show all rank correlation coefficients in Table 2, for data obtained in shadow during each of the 11 event periods. For all the rank correlations,

Table 2. Rank Correlations With Surface Potential Magnitude (Nightside Only)

Event	1	2	3	4	5	6	7	8	9	10	11
N_e	0.135	0.185	−0.404	−0.509	−0.440	0.254	0.558	−0.153	0.026	0.235	0.273
Surface N_e	−0.594	−0.121	−0.819	−0.849	−0.833	−0.070	0.174	−0.406	−0.424	−0.295	−0.393
T_e	0.114	0.149	0.494	0.507	0.542	−0.013	−0.242	0.468	0.362	0.272	−0.097
Surface T_e	0.874	0.604	0.811	0.776	0.839	0.387	0.205	0.755	0.644	0.717	0.369
κ_e	−0.753	−0.243	−0.468	−0.449	−0.406	0.016	−0.007	−0.464	−0.247	−0.580	0.113
J_e	0.224	0.249	−0.319	−0.507	−0.296	0.325	0.591	−0.019	0.161	0.338	0.292
Surface J_e	0.039	0.056	−0.619	−0.817	−0.408	0.173	0.273	−0.033	−0.087	0.131	−0.220
J_i	0.257	0.235	−0.452	−0.542	−0.323	0.480	0.615	0.064	0.243	0.018	0.301
J_e/J_i	−0.046	0.218	0.188	0.031	−0.253	−0.111	0.137	−0.228	−0.192	0.481	0.229
Surface J_e/J_i	−0.276	−0.342	0.079	−0.266	0.002	−0.571	−0.778	−0.142	−0.415	0.033	−0.613
J_{e_hi}	0.767	0.397	0.619	−0.014	0.436	0.374	0.311	0.577	0.632	0.624	0.092
J_{i_hi}	0.638	0.153	−0.475	−0.476	0.104	0.420	0.415	0.465	0.666	−0.558	0.067
J_{e_hi}/J_{i_hi}	0.577	0.246	0.620	0.527	0.422	−0.363	−0.324	0.414	0.565	0.668	0.082
J_{e_hi}/J_e	0.566	−0.012	0.572	0.429	0.550	−0.131	−0.301	0.286	0.342	0.185	−0.163
Surface J_{e_hi}/J_e	0.879	0.385	0.874	0.711	0.779	0.089	0.166	0.505	0.621	0.558	0.196

we have calculated levels of significance. These differ from event to event (because of different time intervals and therefore different numbers of data points), but in general rank correlation coefficients above ~0.2 signify that the correlation has less than a 0.1% chance of arising purely by chance.

[31] We find that none of the parameters measured at spacecraft altitude correlate well with surface potentials for all of the events; however, several parameters correlate closely for almost all of the events. Given the low-energy resolution of the LP ER instrument, we consider the rank correlation coefficients of 0.4–0.6 achieved in many cases reasonably good (they are very statistically significant). For all events except 6, 7, and 11, surface potential magnitude correlates with thermal/suprathermal electron temperature T_E, anti-correlates with kappa index κ_e, and correlates with the ratio of the energetic electron flux to the energetic proton flux (J_{e_hi}/J_{i_hi}). For all events except 2, 6, 7, and 11, the ratio of energetic electron flux to total electron flux (J_{e_hi}/J_e) also correlates with the surface potential magnitude.

[32] All of these correlations (and the lack of consistent correlations for other parameters) make good physical sense. Higher electron temperatures should lead to larger negative surface charging. Lower electron kappa indices imply a more non-Maxwellian distribution with relatively more electron flux at higher energies, which again should lead to larger negative surface charging. Similarly, high levels of energetic electron flux compared to total electron flux or energetic proton flux should both lead to more extreme negative surface charging. Conversely, parameters such as density or total flux (or ratios thereof) might correlate or anti-correlate with the presence of negative surface charging, but should not necessarily correlate directly with the magnitude of the surface potentials. In general, the average energy of the particles should prove more important than their total flux in controlling the magnitude of the surface potential. So the general pattern for most of our event periods corresponds to expectations.

[33] Fluxes at the surface (rather than at spacecraft altitude) should actually more directly control the magnitude of the surface potential. Indeed, when we calculate the corresponding correlation coefficients at the surface, we find that the same general pattern holds, but with even better rank correlation coefficients, consistent with expectations. Unfortunately, we cannot determine a priori whether surface parameters correlate with surface potential because they control the surface potential, or because of the surface potential's effect on the electron distributions that reach the surface. Furthermore, we cannot use these surface parameters for predictive purposes, since we must already know the surface potential in order to calculate them. However, the apparent improved correlation with surface parameters does provide a useful consistency check, suggesting that the fundamental physical processes that control lunar surface charging correspond with our expectations.

[34] Given the consistent pattern followed during most of the event periods, we find it surprising that Events 6, 7, and 11 do not follow a similar pattern. For Events 6 and 11, we observe surface charging only during the peak of the energetic particle fluxes (for Event 6, when a shock front passes the Moon, at 04:00 UT on 08/26). For both of these events, enhanced energetic particle fluxes persist for much longer time periods; however, for whatever reason, only the peak SEP fluxes efficiently charge the lunar surface. During Event 7, meanwhile, enhanced charging correlates most closely with low-energy electron density (and flux) and energetic proton flux, contrary to all expectations.

[35] All electron parameters vary a great deal over each orbit. For instance, electron density decreases and electron temperature increases as the LP spacecraft travels deeper into the lunar wake, because of velocity filtration by the ambipolar potential drop across the wake boundary [*Halekas et al.*, 2005b]. In addition, ambipolar electric fields accelerate solar wind ions into the wake, generating very cold anisotropic beams of ions traveling along magnetic field lines [*Ogilvie et al.*, 1996; *Clack et al.*, 2004]. Therefore we expect surface charging to vary in a complicated way as a function of solar zenith angle on an orbital timescale, as well as on a longer timescale in response to changes in the upstream plasma and energetic particle inputs, and our surface charging observations do indeed bear out these expectations. Our measurements should capture both orbital and longer-term variations in the drivers of surface charging; however, the incomplete data available to us may not adequately represent the full complexity of the orbital variation of the charging currents in the lunar plasma wake, especially those due to ions. We can only speculate that these considerations might partially explain the disparate behavior during some of the event periods discussed above.

Table 3. Rank Correlations With Surface Potential Magnitude (Night and Day) Assuming Sternglass (Upper) or Katz (Lower) Model for Secondary Emission

Event	1	2	3	4	5	6	7	8	9	10	11
Model 0,	0.490	0.152	0.444	0.474	0.422	0.026	−0.327	0.309	0.080	0.298	0.033
DeltaM = 1.1	0.465	0.201	0.512	0.513	0.550	0.018	−0.215	0.342	0.220	0.470	0.022
Model 0,	0.187	0.200	0.167	0.077	0.088	0.033	−0.060	0.216	−0.080	0.227	−0.082
DeltaM = 15	0.263	0.135	0.492	0.498	0.578	−0.012	−0.209	0.352	0.293	0.323	0.024
Model 1,	0.384	0.393	0.615	0.673	0.506	0.114	−0.197	0.363	0.268	0.600	0.001
DeltaM = 1.1	0.470	0.381	0.664	0.609	0.634	−0.006	−0.391	0.339	0.361	0.669	0.005
Model 1,	0.109	0.129	0.229	0.494	0.118	0.150	0.210	0.427	0.151	0.400	0.004
DeltaM = 1.5	0.434	0.370	0.632	0.557	0.661	−0.059	−0.127	0.329	0.324	0.679	0.020
Model 2,	0.430	0.203	0.639	0.659	0.557	0.176	0.004	0.373	0.272	0.504	0.006
DeltaM = 1.1	0.340	0.339	0.647	0.573	0.622	0.203	−0.435	0.394	0.298	0.550	−0.085
Model 2,	0.240	−0.056	0.418	0.356	0.292	0.007	0.153	0.446	0.127	0.318	−0.049
DeltaM = 1.5	0.225	0.224	0.614	0.494	0.605	0.011	−0.103	0.342	0.288	0.499	−0.139

[36] We can confidently predict that the lunar surface will charge to large negative potentials during SEP events. However, it appears that we cannot use any simple measurable quantity (i.e., one easily measured by a lunar orbiter or preferably even with an upstream monitor) to reliably predict the magnitude of the lunar surface potential during any given event. We next investigate whether we can construct a charging model, relying on simple measurable quantities for its inputs, which can do a better job of predicting lunar surface potentials during SEP events.

7. Developing a Predictive Capability

7.1. Models

[37] We consider three models for lunar surface charging. The first, Model 0, has the simplest assumptions. We rely only on LP electron measurements, fitting a kappa function distribution to the electron distribution below 2 keV as in sections 3 and 6 to determine the electron density, temperature, and kappa index (correcting for the spacecraft potential, determined as in section 3). However, whereas for the spacecraft charging calculation we used the full three-dimensional electron distribution, for lunar surface charging modeling we only utilize the downward going portion of the distribution, since only this portion can affect the Moon. We again assume a Maxwellian for the thermal proton distribution, with proton density and temperature equal to the electron values. However, since the Debye length is always very small (<1 km) compared to the size of the Moon, we assume that the thin-sheath charging approximation holds, so that the thermal proton flux does not depend on the surface potential. In other words, $J_I = n_I \sqrt{\frac{kT_I}{2\pi m_I}} \equiv n_{\mathrm{E}} \sqrt{\frac{kT_E}{2\pi m_I}}$, without the (1−eU/kT) factor utilized for the thick-sheath spacecraft case. For Model 0, we do not take into account energetic particles at all.

[38] For Model 0 and subsequent iterations, however, we do consider several different models for secondary emission, with the hope of constructing the best possible charging model for the lunar surface. Indeed, it may prove true that none of the secondary emission yield functions adequately represent the complexity of the lunar environment; however, one model may prove more accurate or useful than others. We therefore consider both Sternglass [*Sternglass*, 1954] and Katz [*Katz et al.*, 1977; *Whipple*, 1981] models for secondary emission. The Sternglass yield function is strictly only appropriate for normal incidence, while the Katz formulation has a slightly more complicated parameterization which depends on the angle of electron incidence. For both formulae, we assume an isotropic incident electron distribution. This has the effect of approximately doubling the secondary emission as compared to normal incidence. For Sternglass emission, we therefore use the secondary yield function

$$\delta(E) = 7.4\delta_M^{eff}(E/E_M)\exp\left(-2\sqrt{E/E_M}\right), \tag{4}$$

with $\delta_M^{\mathrm{eff}} = 2\delta_M^0$. For the Katz formula, we use the angle-integrated version

$$\delta(E) = \frac{2.228\delta_M^0}{Q}(E_M/E)^{0.35}[Q - 1 + \exp(-Q)], \tag{5}$$

with $Q = 2.28(E/E_M)^{1.35}$), which accounts for the isotropic incident distribution. For the same E_M and δ_M^0, the angle-averaged Katz formula predicts secondary emission with a somewhat smaller peak yield (approximately 75% as large), and a peak at a slightly higher energy. In addition, the Katz formula predicts smaller secondary emission below the peak and greater secondary emission at higher energies. In Table 3 and Figures 6–8, we simply list DeltaM = $\delta_M^{\mathrm{eff}} = 2\delta_M^0$, but one should keep in mind the differences between the actual yield functions predicted by the two formulae.

[39] In this study, we test all of our charging models with an E_M of 350 eV and a DeltaM of 1.1 and 1.5 (we have also experimented with larger and smaller yields, but these models clearly do not match the observations). Laboratory experiments with lunar simulants and samples predict a value of ∼3.0 for the electron yield from isotropic incident electron fluxes [*Willis et al.*, 1973; *Horányi et al.*, 1998]. However, measurements from LP of secondary electrons from the lunar regolith suggest a yield from lunar regolith of closer to ∼1.0–1.1 [*Halekas et al.*, 2009] (possibly due to regolith surface roughness effects), consistent with the observation that the lunar surface potential usually remains negative in shadow for a wide range of solar wind conditions.

[40] In order to calculate the predicted lunar surface potential from each of our models, we simply test a range of surface potentials, shifting the electron spectrum by the potential until we find the potential at which the total electron flux to the surface balances the sum of the secondary electron flux and the proton flux. As in section 3, in

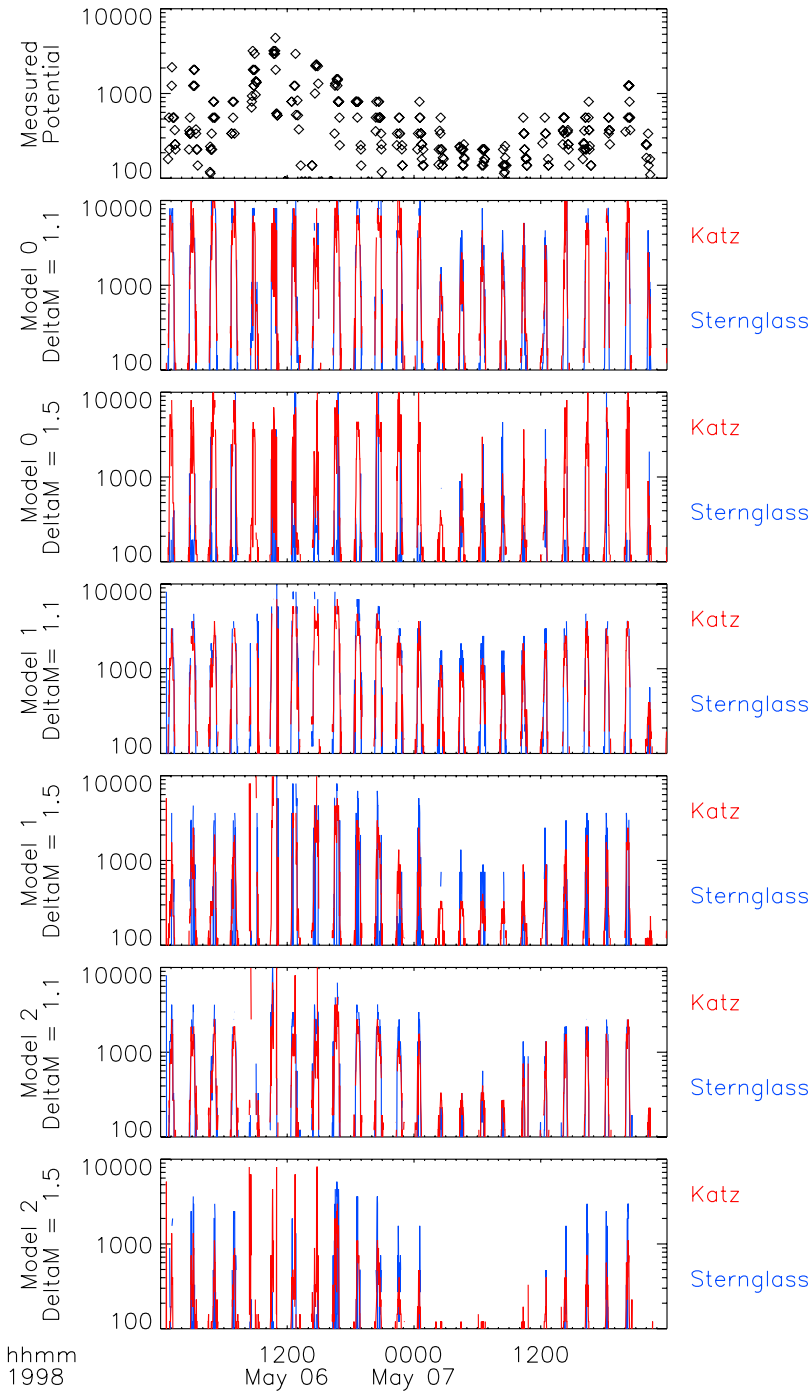

Figure 6. Magnitude of negative lunar surface potentials observed during Event 5, compared to three different surface charging models (described in section 7.1), each calculated for two different secondary emission yield functions and two different effective secondary emission efficiencies (DeltaM = $\delta_M^{\mathrm{eff}} = 2\delta_M^0$). Blue shows Sternglass secondary emission model, red shows Katz secondary emission model.

sunlight we also factor in the additional currents from the solar wind ion flow and the photoelectron flux produced at the surface, with a cosine SZA factor to take into account the angle between the solar wind flow and photon flux and the surface normal. We again assume a solar wind velocity of 400 km/s, but we use a photoemission current of 5 μA/m^2, more appropriate for the lunar surface [*Feuerbacher et al.*, 1972; *Willis et al.*, 1973]. As for the spacecraft, we only consider negative surface charging. For some values of secondary emission, our models do predict small non-negative potentials. In these cases, we can again safely approximate the small positive potentials as zero potential.

[41] For Model 1, we proceed similarly, but also take into account energetic particles, again utilizing upstream measurements from Wind, ACE, and SOHO. We do this exactly as in sections 3 and 6, using upstream measurements to fill in the

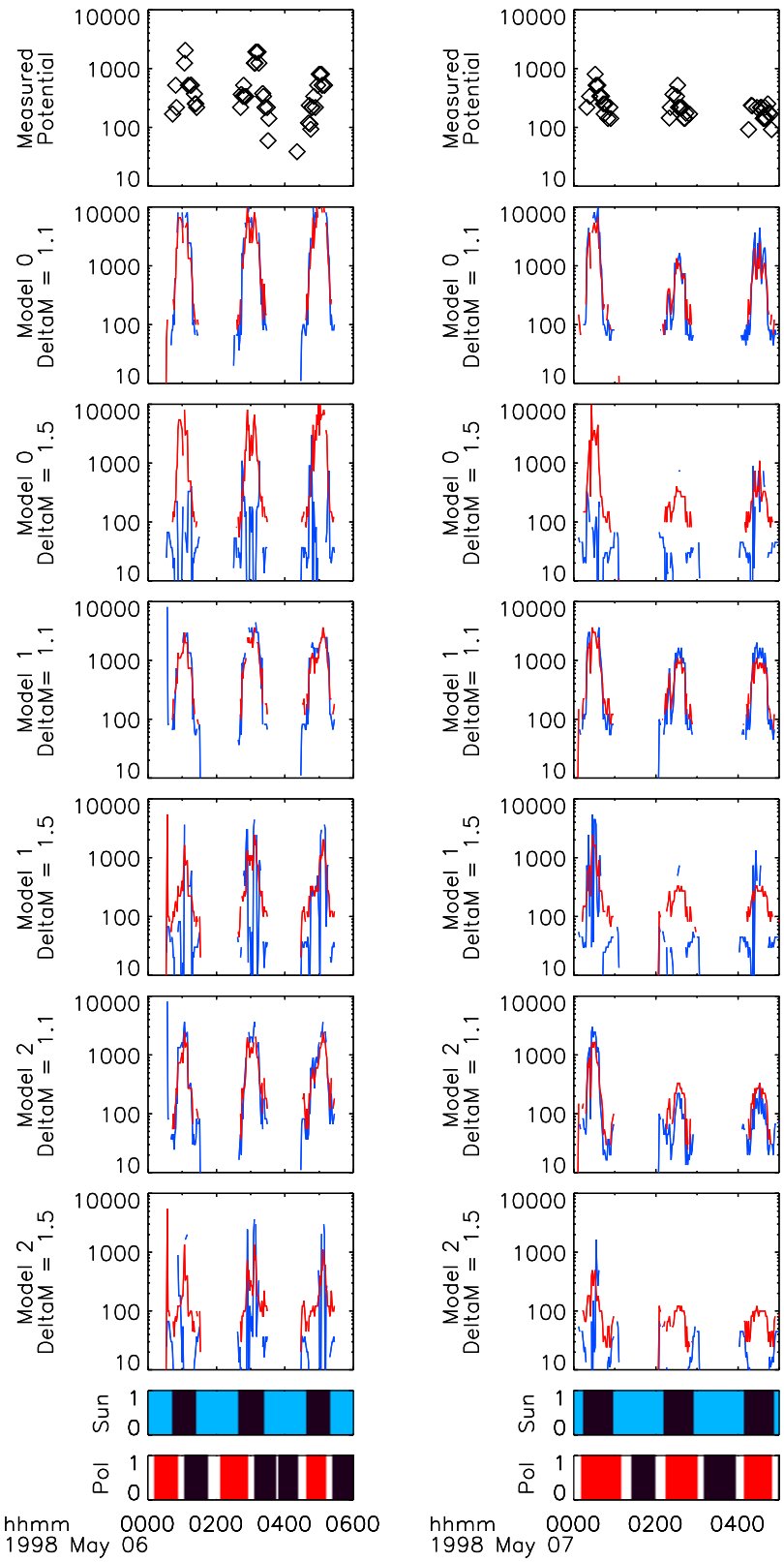

Figure 7. Higher resolution view of two time periods from Figure 6. Top seven images same as in Figure 6. Bottom bars show sun/shadow (blue, sun; black, shadow) and magnetic connection to surface (red, positive polarity; black, negative polarity; white, no connection).

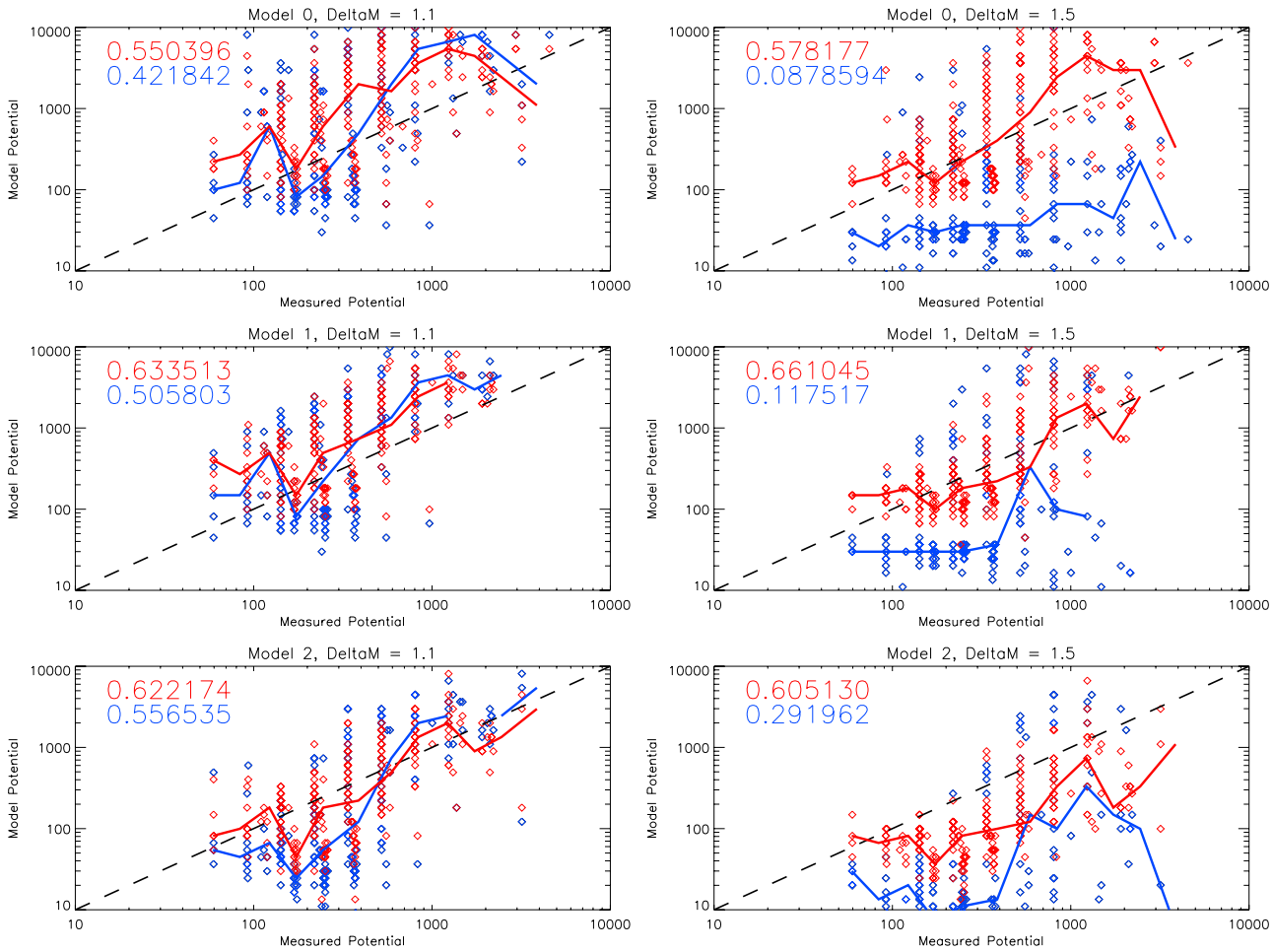

Figure 8. Scatterplots of magnitude of model and measured negative lunar surface potentials for Event 5, for three different surface charging models (described in section 7.1), each calculated for two different secondary emission yield functions and two different secondary emission efficiencies. Dashed line shows one-to-one correspondence, solid colored lines show medians of model potentials for each range of measured potential. Calculated rank correlation coefficients were displayed in upper left part of each image. As in Figures 6 and 7, blue shows Sternglass secondary emission model, red shows Katz secondary emission model.

energetic electron and proton spectra, and extrapolating where necessary to cover the whole energy range from zero to 1 GeV. Other than the addition of these energetic particle fluxes, all calculations remain the same as for Model 0.

[42] As mentioned in the previous section, ions can behave in a complicated fashion in the lunar wake, with ambipolar electric fields accelerating ions into the wake. Our simple model of thermal proton flux may not adequately represent the proton charging currents in the wake. Therefore, in Model 2 we use a slightly more complicated model for the low-energy proton flux in the wake, utilizing the self-similar plasma expansion wake model developed by *Halekas et al.* [2005b]. We can express the thermal proton flux J_{I1} considered up to now in terms of wake model variables (assuming the charged particle density in the wake as a given) using

$$J_{I1} = n\sqrt{\frac{kT_E}{2\pi m_I}} \equiv n\sqrt{\frac{kT_{SW}}{2\pi m_I}}\left[1 + \frac{1}{2\kappa - 2}\sqrt{\frac{2\kappa - 1}{2\kappa - 3}}(Z/C_S + 1)\right]. \tag{6}$$

In equation (6), Z represents the distance from the wake boundary divided by the solar wind convection time past the lunar limb, κ the kappa index of the electron distribution, and the sound speed $C_S = \sqrt{kT_{SW}/m_I}$. Meanwhile, we can use

$$J_{I2} = nV_I \cos\alpha \equiv n\left[Z + \frac{1}{2\kappa - 2}(Z + C_S) + \sqrt{\frac{2\kappa - 3}{2\kappa - 1}}C_S\right]\cos\alpha \tag{7}$$

to calculate the model flux to the surface from ion beams accelerated into the wake by the ambipolar potential, with α the incidence angle between the ion velocity and the surface normal. We assume cylindrically symmetric plasma expansion into the wake, with no asymmetry due to magnetic field orientation. Farther downstream, Wind observations show that the magnetic field does control the wake refilling process to some degree [*Clack et al.*, 2004]. However, at low altitudes, LP electron observations display nearly cylindrical symmetry [*Halekas et al.*, 2005b]. We therefore

use this simpler assumption in our wake expansion model. By comparing the proton fluxes from the two different models (equations (6) and (7)), we can then express the flux expected in the ion beam model J_{I2} in terms of that from thermal flux J_{I1}, resulting in

$$J_{I2} = \left[J_{I1}\sqrt{2\pi}\sqrt{\frac{2\kappa - 3}{2\kappa - 1}} + nZ \right] \cos\alpha. \quad (8)$$

Other than this change to the model for the low-energy proton flux, Model 2 utilizes all the same assumptions as Model 1.

7.2. Model/Data Comparisons

[43] We plot comparisons between measured lunar surface potentials and predictions from all three charging models for Event 5, each for all four different secondary emission yield functions considered, in Figure 6. In Figure 7, we show an expanded view of two smaller time intervals during Event 5, one during a period with extremely large surface charging, and one during a period with more moderate (but still large) charging. We plot all data and model points with negative surface potentials, on both the dayside and night side. For both models and measurements, negative surface potentials can extend some distance sunward of the terminator, due to the glancing incidence and therefore reduced flux to the surface of both solar wind ions and photons near the terminator.

[44] Overall, Model 0 appears to overestimate surface potentials, while Model 1 and 2 come closer to matching the observations. The overestimation by Model 0 appears to be primarily because of the lack of energetic proton fluxes. The total electron fluxes to the surface predicted by Model 0 and Model 1 and 2 are generally similar for all but the largest injections of energetic electrons, with the kappa function fit sometimes overestimating, and sometimes underestimating, the electron flux above several keV. However, the energetic proton fluxes are always larger in Model 1 and 2, generally limiting the surface to smaller negative potentials than predicted by Model 0 in order to keep the electron and proton fluxes balanced. As compared to the spacecraft charging case, energetic electrons and protons prove more important to the charging current balance, and low-energy electrons and protons and secondary electrons less so. The lunar surface has a thin sheath compared to its size, so it cannot attract additional thermal proton flux through the sheath to balance electron currents. Thus, the surface charges to larger negative values than the spacecraft, decreasing the importance of low-energy electrons and secondary electrons, and increasing the relative importance of energetic electrons and protons.

[45] Adding in the effects of energetic particles in Model 1 and 2 improves the performance of our charging model, but adding a more realistic parameterization in Model 2 for the low-energy proton flux in the wake region does not greatly improve the match between model and observations (though it does change the model results appreciably). Protons in the lunar wake may behave in a much more complicated fashion than that predicted by the simple self-similar expansion model used in Model 2. For instance, asymmetries with respect to the magnetic field direction and/or the non-neutral plasma and strong electric fields near the edge of the plasma expansion front predicted by the PIC simulations of *Farrell et al.* [2008] may significantly affect the characteristics of thermal protons in the lunar wake.

[46] For Event 5, at least, Model 1 and Model 2 appear to do an equally good job at predicting the magnitude of the measured potentials, with DeltaM = 1.1 generally better than DeltaM = 1.5, and Katz secondary emission generally better than Sternglass secondary emission. We can confirm this visual impression by plotting scatterplots of model versus measured potentials in Figure 8, and calculating rank correlations. As we concluded above, the scatterplots show that Model 0 consistently overestimates large potentials. Model and 1 and Model 2 both provide a good match to observations, though Model 1 still overestimates large potentials, while Model 2 underestimates smaller potentials to some degree. Model 1 with Katz secondary emission with DeltaM = 1.1–1.5, or Model 2 with Katz secondary emission with DeltaM = 1.1, do the best job of predicting the measured lunar surface potentials for Event 5.

[47] None of the models we considered consistently fit the data for all portions of the LP orbit and all time periods during Event 5. A more complicated model for thermal proton fluxes than we considered in this work might improve this situation, though the increase in sophistication for the proton flux model from Model 1 to Model 2 did not appreciably improve the results. Secondary electron emission yield functions also constitute a great source of uncertainty in our modeling. Perhaps none of the secondary yield functions considered in this study satisfactorily represents the actual physical situation; for instance, the roughness of the lunar regolith may complicate matters in unforeseen ways. Alternatively, one model may prove more accurate in one region or for one type of plasma distribution, while another works better in other regions or for other plasma conditions.

[48] Despite this uncertainty, we can draw some general conclusions about secondary emission. Charging models with Sternglass secondary emission with DeltaM = 1.5 (this secondary emission function has the highest peak yield of any we considered) predict zero or slightly positive potentials in the central wake, where the increased electron temperature ensures enough secondary emission to force the surface potential positive, and therefore these models do not correlate at all well with measurements. The angle-averaged Katz model with DeltaM = 1.1–1.5 and the Sternglass model with DeltaM = 1.1 have peak secondary yields near or not much greater than unity, and these models correlate better with observations. In summary, our measurements strongly disfavor any model with an energy integrated secondary yield greater than unity, or equivalently a peak secondary emission yield larger than $\sim$1.1–1.2, since we usually observe negative potentials even in the central wake during SEP events. This conclusion agrees with previous results from *Halekas et al.* [2008, 2009].

[49] We calculate the same rank correlation coefficients between measurements and models, for all models considered above, for each of our 11 event periods, and show the results in Table 3. Unfortunately, none of our charging models can adequately predict the lunar surface potential for all of the event periods we studied. As for Event 5, Model 1 with Katz secondary emission with DeltaM = 1.1–

1.5 most consistently correlates with the measurements, with Model 2 with DeltaM = 1.1 almost as good. However, consistent with the lack of correlation with basic measurable parameters we found in section 6 during these events, none of our models can successfully predict the lunar surface potential during Events 6, 7, and 11.

7.3. Future Measurement and Model Improvements

[50] In order to more consistently and accurately predict lunar surface charging during SEP events, we will likely need both better measurements of plasma parameters and more sophisticated charging models. The behavior of low-energy protons in the lunar environment presently constitutes the largest uncertainty in our charging models. With actual measurements of proton fluxes in lunar orbit, we could better understand ion behavior in the lunar wake, allowing better predictions of their contribution to surface charging. In the coming years, the SELENE (Kaguya) and ARTEMIS missions should fill this void in our knowledge.

[51] Uncertainties in secondary emission yield functions also contribute to the poor accuracy of our predictions. Laboratory measurements of secondary emission from a bulk lunar regolith sample with realistic charging conditions could solve this issue. In the meantime, measurements of secondary electrons by LP [*Halekas et al.*, 2009] may provide the best available estimate of in situ lunar secondary emission. Variability in secondary emission yields from different regions of the surface or changes due to temperature variations could also affect lunar surface charging. Finally, secondary electron emission from ion impact, which we did not consider at all in this study, may significantly contribute to the charging balance.

[52] Better characterization of energetic particle behavior in the lunar environment would also improve our understanding of lunar charging during SEP events. We have assumed energetic particle fluxes at lunar orbit equal to those measured by upstream monitors. However, the lunar environment may perturb and/or attenuate energetic particle fluxes to some degree, especially during time periods with very anisotropic SEP fluxes. In addition, the behavior of heavier ions (not considered in this study) may prove important, both as primary fluxes and as producers of secondaries.

[53] Finally, improved measurements of lunar surface potentials would allow us to better calibrate our charging models, and thereby better predict lunar charging during SEP events. The poor energy resolution of the LP ER instrument limits the resolution of our surface potential measurements. In addition, the LP spacecraft potential may represent a significant source of error. We have made every attempt to accurately determine the spacecraft potential, but the spacecraft potential may still differ from our expectations at times. Given that we use a similar procedure to determine the spacecraft potential and model the surface potential, we certainly must admit the possibility that we may underestimate or overestimate the spacecraft potential at times, especially during extreme conditions like those encountered during SEP events. The spacecraft is small compared to the Debye scale and likely has a higher secondary electron emission yield, both of which should limit the spacecraft potential to much smaller values than the surface potential. However, at some times, the spacecraft could still charge to a larger potential than we expect, which would in turn change our estimates of the surface potential. Electron data from an instrument with better energy resolution, on a spacecraft with a way to directly determine or better predict the spacecraft potential, would allow better quantitative measurements of lunar surface charging. These would in turn allow us to develop better models to predict lunar potentials during SEP events (and, indeed, at all times).

8. Implications

[54] SEP events will certainly present a hazard to lunar explorers, due to the high levels of penetrating radiation. However, given the large lunar surface potentials we observe during SEP events, robotic and/or human explorers may also encounter additional hazards associated with electrostatic discharge and/or dust effects. Though we do not yet fully understand the level of risk associated with these phenomena, if they do prove hazardous for surface exploration we will need to develop the capability to predict the magnitude of surface charging expected during any given SEP event. This study shows that, with an appropriate plasma monitor in place, we could currently achieve this goal for some events, but not all. To develop a consistent and reliable predictive capability, we will need to know more about the lunar environment and its effects on both low-energy and energetic charged particle distributions. Luckily, in the coming years a number of missions, including ARTEMIS and Kaguya, should begin to fill in these voids in our knowledge.

[55] **Acknowledgments.** This work was supported by NASA grants NNG06GJ23G and NNX07AG10G. We thank the ACE EPAM and SIS instrument teams, the Wind EPACT team, the SOHO COSTEP instrument team, and NASA's CDAWEB for providing energetic particle data.

[56] Wolfgang Baumjohann thanks Tomoko Nakagawa and Yoshifumi Saito for their assistance in evaluating this paper.

References

Adams, J. H., Jr., and M. M. Shapiro (1985), Irradiation of the Moon by galactic cosmic rays and other particles, in *Lunar Bases and Space Activities of the 21st Century Conference*, pp. 315–327, Lunar and Planet. Inst., Houston, Tex.

Alvarez, R. (1977), Photoconductive effects on lunar and terrestrial fines, *Proc. Lunar Sci. Conf. 8th*, *1*, 277–1290.

Bedingfield, K. L., R. D. Leach, and M. B. Alexander (1996), Spacecraft system failures and anomalies attributed to the natural space environment, *NASA Ref. Publ., 1390*, NASA, Marshall Space Flight Cent., Ala.

Burlaga, L. F., R. M. Skoug, C. W. Smith, D. F. Webb, T. H. Zurbuchen, and A. Reinard (2001), Fast ejecta during the ascending phase of solar cycle 23: ACE observations, 1998–1999, *J. Geophys. Res.*, *106*, 20,957–20,977.

Clack, D., J. C. Kasper, A. J. Lazarus, J. T. Steinberg, and W. M. Farrell (2004), Wind observations of extreme ion temperature anisotropies in the lunar wake, *Geophys. Res. Lett.*, *31*, L06812, doi:10.1029/2003GL018298.

Farrell, W. M., T. J. Stubbs, J. S. Halekas, G. T. Delory, M. R. Collier, R. R. Vondrak, and R. P. Lin (2008), Loss of solar wind plasma neutrality and affect on surface potentials near the lunar terminator and shadowed polar regions, *Geophys. Res. Lett.*, *35*, L05105, doi:10.1029/2007GL032653.

Farrugia, C. J., et al. (2002), Wind and ACE observations during the great flow of 1–4 May 1998: Relation to solar activity and implications for the magnetosphere, *J. Geophys. Res.*, *107*(A9), 1240, doi:10.1029/2001JA000188.

Feuerbacher, B., M. Anderegg, B. Fitton, L. D. Laude, R. F. Willis, and R. J. L. Grard (1972), Photoemission from lunar surface fines and the lunar photoelectron sheath, *Proc. Lunar Sci. Conf.*, *3*, 2655–2663.

Gold, R. E., S. M. Krimigis, S. Hawkins III, E. Haggerty, D. K. Lohr, D. A. Fiore, E. Armstrong, T. P. Holland, and G. Lanzerotti (1998), Electron, proton, and alpha monitor on the advanced composition explorer, *Space Sci. Rev.*, *86*, 541–562.

Halekas, J. S., D. L. Mitchell, R. P. Lin, L. L. Hood, M. H. Acuña, and A. B. Binder (2002), Evidence for negative charging of the lunar surface in shadow, *Geophys. Res. Lett.*, *29*(10), 1435, doi:10.1029/2001GL014428.

Halekas, J. S., R. P. Lin, and D. L. Mitchell (2003), Inferring the scale height of the lunar nightside double layer, *Geophys. Res. Lett.*, *30*(21), 2117, doi:10.1029/2003GL018421.

Halekas, J. S., R. P. Lin, and D. L. Mitchell (2005a), Large negative lunar surface potentials in sunlight and shadow, *Geophys. Res. Lett.*, *32*, L09102, doi:10.1029/2005GL022627.

Halekas, J. S., S. D. Bale, D. L. Mitchell, and R. P. Lin (2005b), Magnetic fields and electrons in the lunar plasma wake, *J. Geophys. Res.*, *110*, A07222, doi:10.1029/2004JA010991.

Halekas, J. S., G. T. Delory, D. A. Brain, R. P. Lin, M. O. Fillingim, C. O. Lee, R. A. Mewaldt, T. J. Stubbs, W. M. Farrell, and M. K. Hudson (2007), Extreme lunar surface charging during solar energetic particle events, *Geophys. Res. Lett.*, *34*, L02111, doi:10.1029/2006GL028517.

Halekas, J. S., G. T. Delory, R. P. Lin, T. J. Stubbs, and W. M. Farrell (2008), Lunar Prospector observations of the electrostatic potential of the lunar surface and its response to incident currents, *J. Geophys. Res.*, *113*, A09102, doi:10.1029/2008JA013194.

Halekas, J. S., G. T. Delory, R. P. Lin, T. J. Stubbs, and W. M. Farrell (2009), Lunar Prospector measurements of secondary electron emission from lunar regolith, *Planet. Space Sci.*, *57*, 78–82, doi:10.1016/j.pss.2008.11.2009.

Horányi, M. (1996), Charged dust dynamics in the solar system, *Annu. Rev. Astron. Astrophys.*, *34*, 383–418.

Horányi, M., B. Walch, S. Robertson, and D. Alexander (1998), Electrostatic charging properties of Apollo 17 lunar dust, *J. Geophys. Res.*, *103*, 8575–8580.

Howard, T. A., and S. J. Tappin (2005), Statistical survey of earthbound interplanetary shocks, associated coronal mass ejections and their space weather consequences, *Aston. Astrophys.*, *440*, 373–383, doi: 10.1051/0004-6361:20053109.

Katz, I., D. E. Parks, M. J. Mandell, J. M. Harvey, D. H. Brownell, S. S. Wang, and M. Rotenberg (1977), A three dimensional dynamic study of electrostatic charging in materials, *NASA CR-135256*, NASA.

Kahler, S. W. (2005), Characteristic times of gradual solar energetic particle events and their dependence on associated coronal mass ejections, *Astrophys. J.*, *628*, 1014–1022.

Koons, H. C., J. E. Mazur, R. S. Selesnick, J. B. Blake, J. F. Fennell, J. L. Roeder, and P. C. Anderson (2000), The impact of the space environment on space systems, in *6th Spacecr. Charging Technol. Conf.*, *AFRL-VS-TR-20001578*, pp. 7–10.

Leach, R. D. (1995), Spacecraft system failures and anomalies attributed to the natural space environment, *AIAA 1995 Space Programs and Technologies Conference*, AIAA, Washington, D.C.

Malandraki, O. E., E. T. Sarris, L. J. Lanzerotti, P. Trochoutsos, G. Tsiropoula, and M. Pick (2002), Solar energetic particles inside a coronal mass ejection event observed with the ACE spacecraft, *J. Atmos. Sol. Terr. Phys.*, *64*, 517–525.

Manka, R. H. (1973), Plasma and potential at the lunar surface, in *Photon and Particle Interactions With Surfaces in Space*, edited by R. J. L. Grard, pp. 347–361, D. Reidel, Dordrecht, Netherlands.

Muller-Mellin, R., et al. (1995), COSTEP—Comprehensive Suprathermal and Energetic Particle Analyser, *Sol. Phys.*, *162*, 483–504.

Ogilvie, K. W., J. T. Steinberg, R. J. Fitzenreiter, C. J. Owen, A. J. Lazarus, W. M. Farrell, and R. B. Torbert (1996), Observations of the lunar plasma wake from the WIND spacecraft on December 27, 1994, *Geophys. Res. Lett.*, *23*, 1255–1258.

Press, W. H., S. A. Teukolsky, W. T. Vetterling, and B. P. Flanney (1992), *Numerical Recipes in Fortran: The Art of Scientific Computing*, 2nd ed., Cambridge Univ. Press, Cambridge, U. K.

Schwerer, F. C., G. P. Huffman, R. M. Fisher, and T. Nagata (1974), Electrical conductivity of lunar surface rocks: Laboratory measurements and implications for lunar interior temperatures, *Proc. Lunar Sci. Conf. 5th*, *2*, 673–2687.

Sternglass, E. J. (1954), The theory of secondary emission, *Sci. Pap. 1772*, Westinghouse Res. Lab., Pittsburgh, Pa.

Stone, E. C., et al. (1998), The solar isotope spectrometer for the advanced composition explorer, *Space Sci. Rev.*, *86*, 357–408.

Stubbs, T. J., R. R. Vondrak, and W. M. Farrell (2006), A dynamic fountain model for lunar dust, *Adv. Space Res.*, *37*(1), 59–66.

Stubbs, T. J., R. R. Vondrak, and W. M. Farrell (2007a), Impact of dust on lunar exploration, in *Dust in Planetary Systems*, (Workshop, 26–30 September 2005, Kauai, HI), edited by H. Krüger and A. L. Graps, pp. 239–244, *ESA Publ., SP-643*, ESTEC, Noordwijk, Netherlands.

Stubbs, T. J., J. S. Halekas, W. M. Farrell, and R. R. Vondrak (2007b), Lunar surface charging: A global perspective using Lunar Prospector data, in *Dust in Planetary Systems*, (Workshop, 26–30 September 2005, Kauai, HI), edited by H. Krüger and A. L. Graps, pp. 181–184, *ESA Publ., SP-643*, ESTEC, Noordwijk, Netherlands.

Stubbs, T. J., R. R. Vondrak, and W. M. Farrell (2007c), A dynamic fountain model for dust in the lunar exosphere, in *Dust in Planetary Systems*, (Workshop, 26–30 September 2005, Kauai, HI), edited by H. Krüger and A. L. Graps, pp. 185–190, *ESA Publ., SP-643*, ESTEC, Noordwijk, Netherlands.

Torsti, J., E. Riihonen, and L. Kocharov (2004), The 1998 May 2–3 magnetic cloud: An interplanetary "highway" for solar energetic particles observed with SOHO/ERNE, *Astrophys. J.*, *600*, L83–L86.

von Rosenvinge, T. T., et al. (1995), The energetic particles: Acceleration, composition, and transport (EPACT) investigation on the Wind spacecraft, *Space Sci. Rev.*, *71*, 155–206.

von Rosenvinge, T. T., et al. (2000), The solar energetic particle event of 6 May 1998, in *Acceleration and Transport of Energetic Particles Observed in the Heliosphere*, edited by R. A. Mewaldt et al., pp. 111–114, AIP.

Whipple, E. C. (1981), Potentials of surfaces in space, *Rep. Prog. Phys.*, *44*, 1197–1250.

Willis, R. F., M. Anderegg, B. Feuerbacher, and B. Fitton (1973), Photoemission and secondary electron emission from lunar surface material, in *Photon and Particle Interactions with Surfaces in Space*, edited by R. J. L. Grard, pp. 389–401, D. Reidel, Dordrecht, Netherlands.

G. T. Delory, J. S. Halekas, and R. P. Lin, Space Sciences Laboratory, University of California, 7 Gauss Way, Berkeley, CA 94720, USA. (jazzman@ssl.berkeley.edu)

W. M. Farrell, Solar System Exploration Department, NASA Goddard Spaceflight Center, Code 690, Greenbelt, MD 20771, USA.

T. J. Stubbs, Heliophysics Division, NASA Goddard Space Flight Center, Code 674, Greenbelt, MD 20771, USA.